Journal of Nanobiotechnology

RESEARCH

Open Access

Targeted blood-brain barrier penetration and precise imaging of infiltrative glioblastoma margins using hybrid cell membrane-coated ICG liposomes

Ping Liu[1†], Siyi Lan[2†], Duyang Gao[2,3], Dehong Hu[2,3], Zhen Chen[2], Ziyue Li[2], Guihua Jiang[1*] and Zonghai Sheng[2,3*]

Abstract

Surgical resection remains the primary treatment modality for glioblastoma (GBM); however, the infiltrative nature of GBM margins complicates achieving complete tumor removal. Additionally, the blood-brain barrier (BBB) poses a formidable challenge to effective probe delivery, thereby hindering precise imaging-guided surgery. Here, we introduce hybrid cell membrane-coated indocyanine green (ICG) liposomes (HM-Lipo-ICG) as biomimetic near-infrared (NIR) fluorescent probes for targeted BBB penetration and accurate delineation of infiltrative GBM margins. HM-Lipo-ICG encapsulates clinically approved ICG within its core and utilizes a hybrid cell membrane exterior, enabling specific targeting and enhanced BBB permeation. Quantitative assessments demonstrate that HM-Lipo-ICG achieves BBB penetration efficiency 2.8 times higher than conventional ICG liposomes. Mechanistically, CD44 receptor-mediated endocytosis facilitates BBB translocation of HM-Lipo-ICG. Furthermore, HM-Lipo-ICG enables high-contrast NIR imaging, achieving a signal-to-background ratio of 6.5 in GBM regions of an orthotopic glioma mouse model, thereby improving tumor margin detection accuracy fourfold (84.4% vs. 22.7%) compared to conventional ICG liposomes. Application of HM-Lipo-ICG facilitates fluorescence-guided precision surgery, resulting in complete resection of GBM cells. This study underscores the potential of hybrid cell membrane-coated liposomal probes in precisely visualizing and treating infiltrative GBM margins.

Introduction

Glioblastoma (GBM) is a primary brain tumor characterized by exceptionally high malignancy, mortality, and recurrence rates, invariably associated with a poor prognosis [1]. Despite various treatment modalities such as radiotherapy, chemotherapy, and immunotherapy, surgical resection remains the preferred and most effective strategy currently available [2]. Difficulties in distinguishing the margins between occult tumors and healthy tissue during surgical removal often led to incomplete excision and inefficient surgery [3]. The importance of achieving maximal tumor resection for GBM survival underscores the urgent need for clear identification and

†Ping Liu and Siyi Lan contributed equally to this work.

*Correspondence:
Guihua Jiang
13828472201@163.com
Zonghai Sheng
zh.sheng@siat.ac.cn

Full list of author information is available at the end of the article

Graphical abstract

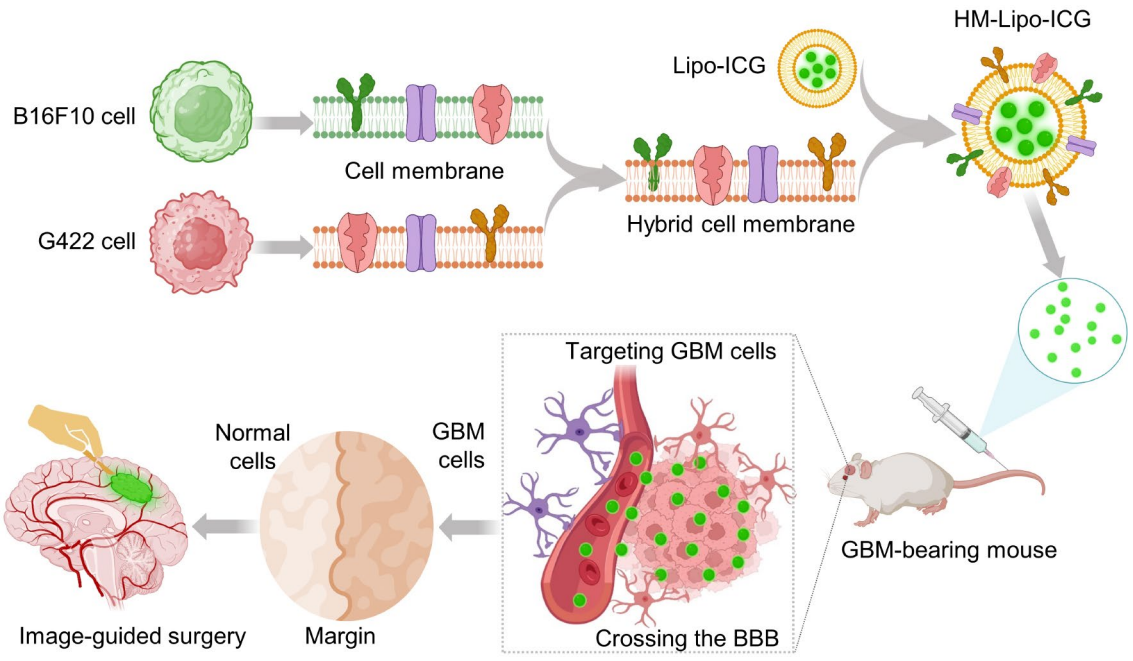

Keywords Glioblastoma, Tumor margin, Indocyanine green, Fluorescence, Cell membrane

visualization of the infiltrative tumor margin [4, 5]. Currently, intraoperative optical technologies, including exoscopy, fluorescence [6, 7], and Raman spectroscopy [8–10], have emerged as promising approaches to detecting and localizing the invasive margin of GBM [3, 11]. In particular, the fluorophore indocyanine green (ICG) offers the advantage of fluorescence imaging in the near-infrared (NIR) window, allowing visualization of tumor margins [12, 13]. However, ICG faces challenges related to its inefficient blood-brain barrier (BBB) penetration, limited tumor targeting, and short half-life in the circulatory system [14, 15], which restrict its applicability for precise visualization of tumor margins in GBM.

Liposomes, serving as clinically used drug delivery systems [16], have demonstrated the ability to raise the stability and prolong the systemic circulation half-life of ICG [17–19]. Additionally, liposome-encapsulated ICG (Lipo-ICG) not merely sustains the metabolic pathway of ICG but also shows potential application in clinical practice [20]. With the innate ability to passively target tumor regions through the enhanced permeability and retention (EPR) effect, Lipo-ICG exhibits enhanced accumulation of ICG at tumor sites [21]. Furthermore, the bilayer molecular membrane structure of liposomes offers the prospect of spontaneous fusion with cell membranes [18, 21, 22]. These properties endow liposomes with natural biological functionalities and targeting capabilities [23], but they also suffer from limited temporal colloidal stability, uncontrolled release, and the need for custom-synthesized phospholipids.

The advent of the biomimetic approach proposed by Zhang et al. [24]. has driven the application of cell membrane-camouflaged nanoparticles in various tumor models [25, 26], improving the diagnosis and treatment of GBM [27–29]. Biomimetic nanoprobes based on cancer cell membranes exhibit exceptional homotypic binding, BBB penetration [30], and immune escape functionalities [31]. However, the inherent complexity of tumor characteristics renders monotypic cell membranes insufficient to meet the diverse and stringent requirements of biomedical applications. The emerging hybrid cell membrane (HM) coating approach has paved the way for addressing these specific applications, acquiring functionalities from both source cell membranes [32, 33]. This unique design not only retains the physicochemical features of the nanoparticle but also achieves homotypic targeting coupled with exceptional long-term circulation performance [34]. Studies with specific cancer cell types, such as B16F10 (murine melanoma cells), have demonstrated the potential to cross the BBB due to their high metastatic ability to the brain [35–38]. Theoretically, an elaborately designed HM holds the promise of simultaneously utilizing two biological functions—BBB penetration and GBM targeting—derived from the constituent

cell membranes [39]. This custom dual-functional liposomal probe, modified with a fusion cell membrane, holds the potential for the precise visualization of infiltrative margins of GBM.

Herein, we propose an HM-camouflaged ICG liposome, termed HM-Lipo-ICG, which possesses both the physical and chemical functions of the nanocarrier itself and the cell membranes' biological functionalities. The HM consists of B16F10 cell membrane (BM) and G422 (glioblastoma cell, GM) cell membranes, imparting outstanding BBB-crossing ability and homologous tumor-targeting capabilities from their source cell membranes (Scheme 1). By utilizing the NIR fluorescence of ICG, the constructed HM-coated liposomes achieve more effective and precise visualization of the infiltrative margin of GBM as compared with Lipo-ICG. The application of these nanoprobes enables the image-guided maximal resection of orthotopic glioma. This innovative strategy holds the potential to enhance precise tumor lesion visualization and minimize residual margins in GBM, thereby mitigating postoperative recurrence and extending survival for patients with GBM.

Results and discussion

Preparation and characterization of HM-Lipo-ICG

Lipo-ICG was prepared using a thin-layer hydration method [22, 40]. Cell membranes from B16F10 and G422 GBM cells were isolated and integrated into Lipo-ICG through continuous physical extrusion, resulting in the formation of HM-Lipo-ICG [24, 41]. Transmission electron microscopy (TEM) images revealed uniform spherical shapes with nanoshells of a protein corona in HM-Lipo-ICG, contrasting with Lipo-ICG, confirming successful membrane integration (Fig. 1A, B). Dynamic light scattering (DLS) measurements indicated a smaller hydrated dynamic size for HM-Lipo-ICG (98.8±0.8 nm, PDI=0.145) compared to Lipo-ICG (117.6±4.6 nm, PDI=0.191), attributed to physical compression during membrane modification (Fig. 1C, Fig. S1). HM-Lipo-ICG maintained stable hydrodynamic size in water, phosphate-buffered solution (PBS), and 10% fetal bovine serum (FBS) over 10 days, demonstrating excellent stability (Fig. S2). The zeta potential of HM-Lipo-ICG (-36.3±1.0 mV) was higher than that of Lipo-ICG (-45.6±0.4 mV) (Fig. S3), indicating surface potential alteration due to membrane incorporation (-37.3±2.9 mV). SDS-polyacrylamide gel electrophoresis (SDS-PAGE) confirmed the presence of primary protein bands from B16F10 and G422 cell membranes in the HM-Lipo-ICG band (Fig. 1D), verifying successful membrane fusion. Furthermore, dual-channel fluorescence microscopy of FITC and Cy5 dye-labeled membranes showed high overlap in HM-Lipo-ICG aggregates (Fig. 1E), confirming successful co-modification. The encapsulation efficiency and the loading capacity of ICG in HM-Lipo-ICG were calculated to be 77.6±3.7% and 3.7% ± 0.2%, respectively.

The photophysical properties of HM-Lipo-ICG were investigated. UV-vis-NIR absorption and fluorescence spectra were similar to free ICG (Fig. 1F, G), indicating

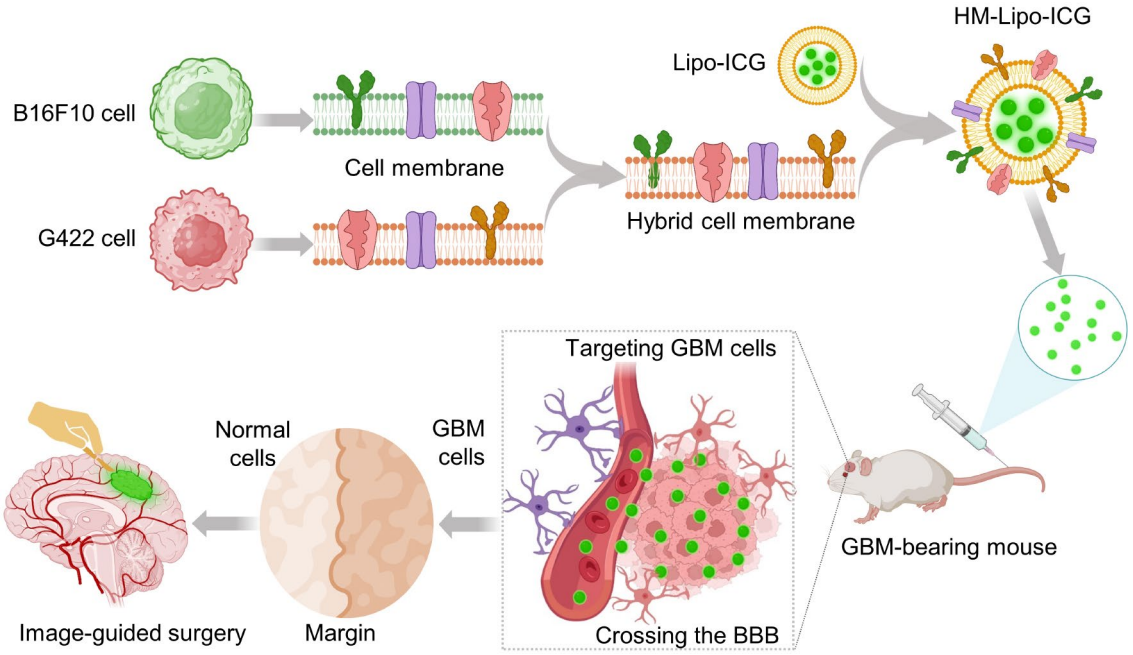

Scheme 1 Schematic depiction of the preparation process for HM-Lipo-ICG and its utilization in NIR fluorescence imaging of GBM-bearing mice, encompassing tumor margin delineation and guidance for surgical resection. Image was created with BioRender.com, with permission

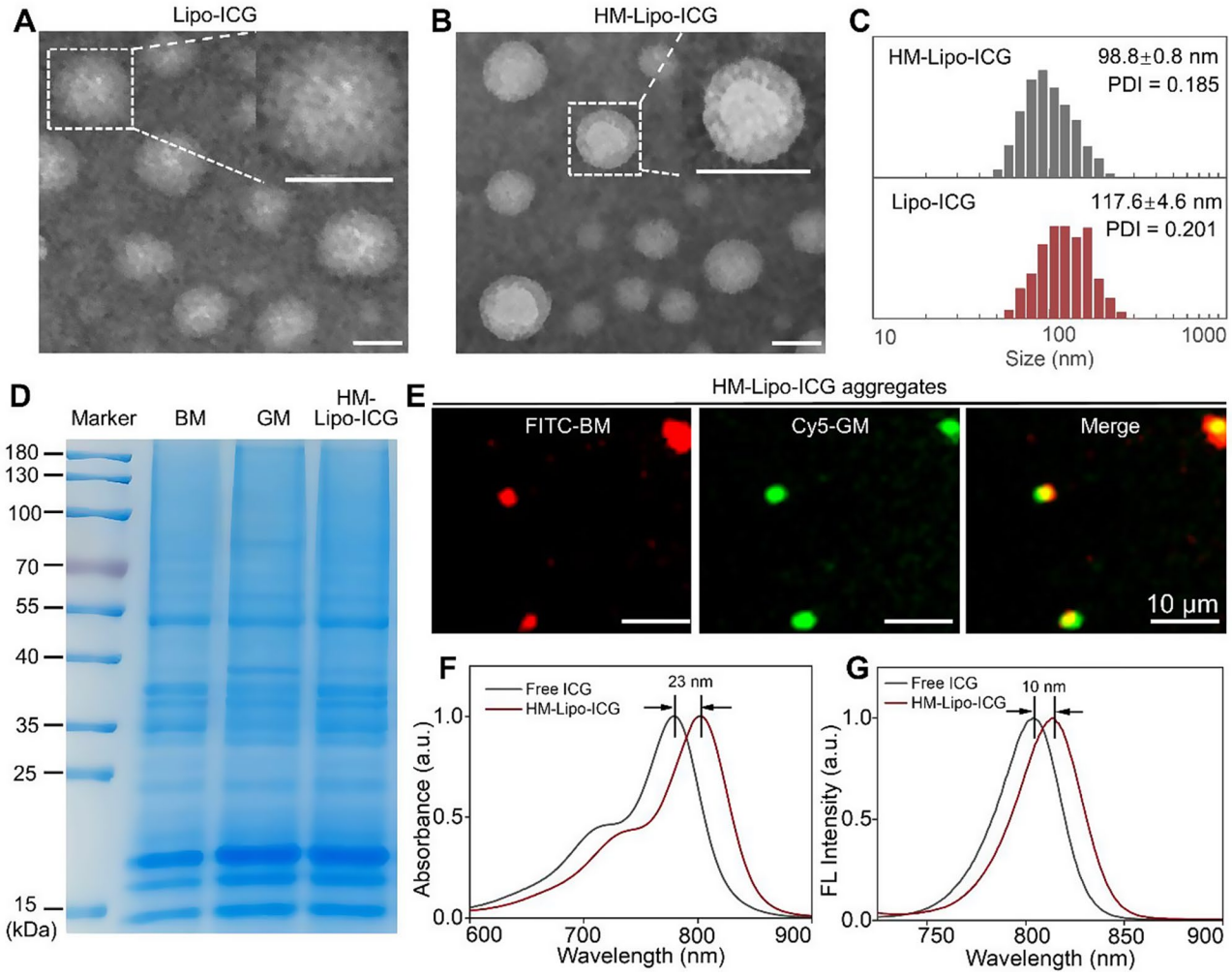

Fig. 1 Characterization of HM-Lipo-ICG. **a**) TEM images of Lipo-ICG and **b**) HM-Lipo-ICG. Samples were negatively stained with phosphotungstic acid. Insets display a magnified view of a single liposome. Scale bar = 100 nm. **c**) Hydrodynamic diameter of Lipo-ICG and HM-Lipo-ICG measured by DLS. **d**) SDS-PAGE protein analysis of marker, B16F10 cell membrane (BM), G422 cell membrane (GM), and HM-Lipo-ICG. **e**) Fluorescence microscopy images of HM-Lipo-ICG aggregates with FITC-labelled B16F10 cell membrane (red) and Cy5-labelled G422 cell membrane (green). Scale bar = 10 μm. HM-Lipo-ICG with 50 μL at a concentration of 0.1 mg/mL was added dropwise to slides and allowed to dry at room temperature under light-protected conditions. **f**) Normalized absorption spectra and **g**) fluorescence spectra of free ICG and HM-Lipo-ICG. $C_{ICG} = C_{HM-Lipo-ICG} = 20$ μg/mL

no chemical alteration due to the hybrid membrane coating strategy [19]. However, an absorption peak redshift from 780 nm to 803 nm (Fig. 1F) and a fluorescence intensity redshift from 804 nm to 814 nm (Fig. 1G) was observed, attributed to free ICG encapsulation in the liposome's hydrophilic core.

Optical stability assessment showed a significant improvement in HM-Lipo-ICG, with only a 20% reduction in fluorescence intensity compared to a 65% reduction in free ICG after 6 days of storage (Fig. S4), highlighting enhanced stability conferred by liposomal encapsulation.

In Vitro targeted BBB penetration of HM-Lipo-ICG

The CD44 protein on the surface of B16F10 cells [42, 43] can specifically interact with the hyaluronic acid (HA) on the surface of bEnd.3 cells [36, 44]. Therefore, the CD44 marker on the HM-Lipo-ICG was further detected by western-blotting(WB) measurements. The expression of CD44 in both the BM-Lipo-ICG and HM-Lipo-ICG (Fig. S5) was detected, suggesting that the HM-Lipo-ICG inheritated the marker proteins from source cells.

We hypothesized that Lipo-ICG modified with B16F10 cell membranes would enhance cellular uptake, thereby promoting HM-Lipo-ICG's ability to cross the BBB *via* receptor-mediated endocytosis [44]. To investigate this, we first assessed the uptake of HM-Lipo-ICG by bEnd.3 cells using confocal fluorescence imaging and flow

cytometry. Results indicated a higher ICG fluorescence signal in the HM-Lipo-ICG-treated group compared to the Lipo-ICG-treated group. Conversely, in the CD44 antibody-blocked group, the ICG signal in bEnd.3 cells was significantly reduced compared to the HM-Lipo-ICG-treated group (Fig. 2A). Flow cytometry quantitative analysis revealed that the mean fluorescence intensity of the HM-Lipo-ICG-treated group was 1.5 times higher than that of the Lipo-ICG-treated group and 1.4 times higher than that of the CD44 antibody-blocked group (Fig. 2B, C). This result indicates that fusion cell membrane modification enhances the uptake efficiency of Lipo-ICG by bEnd.3 cells, and this enhancement is

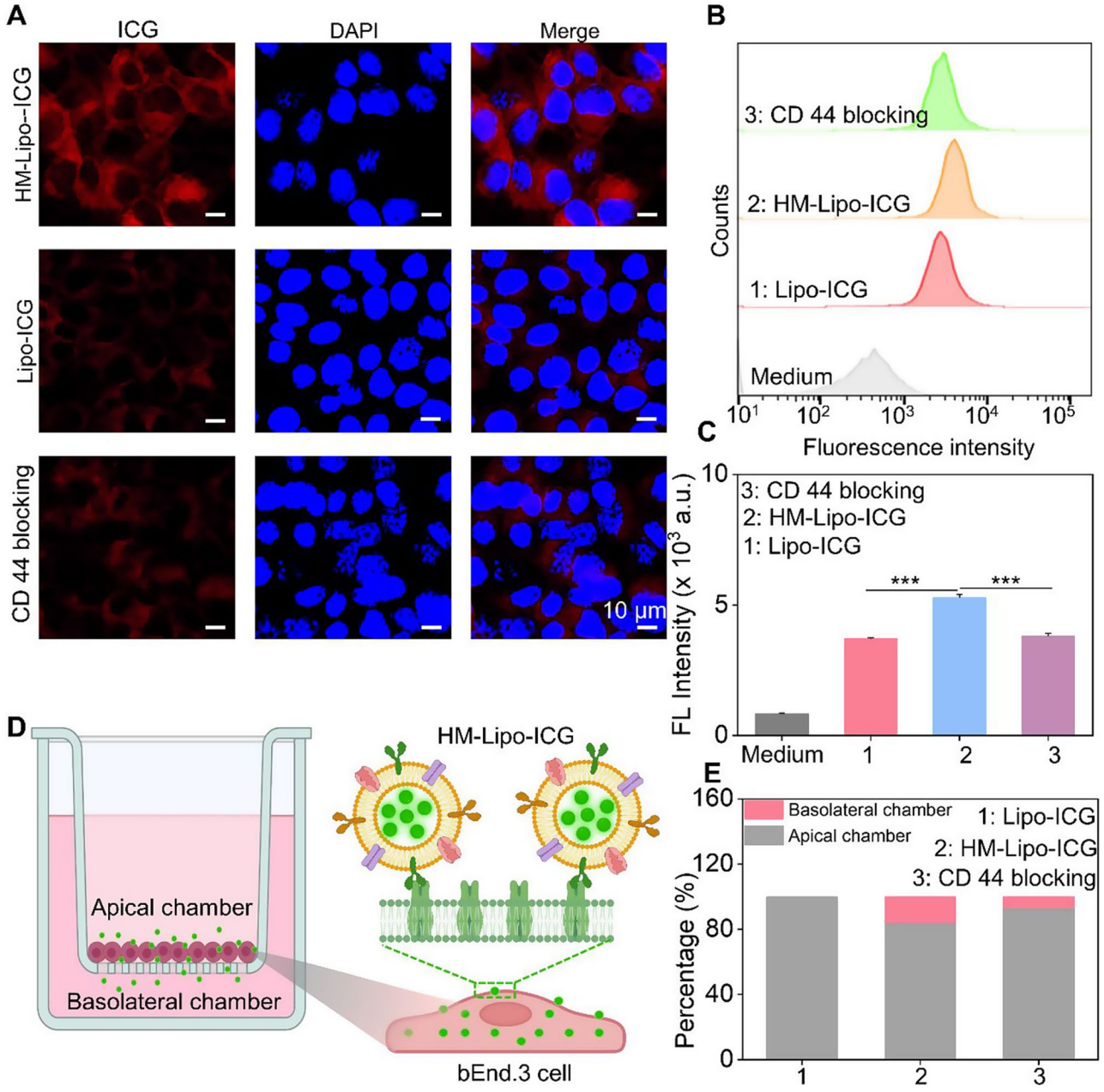

Fig. 2 In vitro evaluation of HM-Lipo-ICG for crossing the BBB. **a**) CLSM images of bEnd.3 cells incubated for 4 h with Lipo-ICG, HM-Lipo-ICG NPs, and HM-Lipo-ICG NPs pre-blocked with CD44 antibody. $C_{ICG} = C_{Lipo-ICG} = C_{HM-Lipo-ICG} = 20$ μg/mL. The cell nuclei were stained by DAPI. Scale bar = 10 μm. **b**) Flow cytometry quantification of bEnd.3 cell uptake of Lipo-ICG, HM-Lipo-ICG, and HM-Lipo-ICG following CD44 antibody blocking. **c**) Quantitative analysis of the average fluorescent intensity of ICG in Fig. 2B. Data denote mean ± s.d, *** $P < 0.001$, $n = 3$. **d**) Schematic of the in vitro Transwell model. The inset illustrates the mechanism by which HM-Lipo-ICG crosses the BBB through receptor-mediated endocytosis. **e**) Quantitative analysis of the ability of Lipo-ICG, HM-Lipo-ICG and HM-Lipo-ICG pre-blocked with CD44 antibody to traverse the in vitro BBB model ($n = 3$). The amount of ICG in the upper and lower chambers was measured and calculated using a linear standard curve

closely related to the specific interaction between the HA on bEnd.3 cells and CD44 on B16F10 cell membranes.

Next, an in vitro BBB Transwell model [44] was established using bEnd.3 cells to preliminarily evaluate the ability of HM-Lipo-ICG to traverse the BBB (Fig. 2D). The trans-endothelial electrical resistance (TEER) of the BBB Transwell model was measured to confirm model reliability (data not shown). Results showed that the relative proportion of ICG in the apical chamber of the HM-Lipo-ICG-treated group (80.8%) was lower than that of the Lipo-ICG (100%) and CD44 blocking groups (91.2%) (Fig. 2E). Conversely, the proportion of ICG in the basolateral chamber of the HM-Lipo-ICG-treated group (19.2%) was higher than that of the Lipo-ICG (0%) and CD44 blocking groups (8.8%) (Fig. 2E). This confirms that fusion cell membrane significantly enhances the ability of Lipo-ICG to traverse the in vitro BBB.

Homotypic targeting of HM-Lipo-ICG to glioma cells in Vitro

Before assessing the homologous targeting performance of HM-Lipo-ICG, its cytotoxicity to G422 GBM cells and bEnd.3 cells was evaluated using the Cell Counting Kit-8 (CCK-8) assay (Fig. S6). The results demonstrated that HM-Lipo-ICG exhibits high cell viability even at an ICG concentration of 40 μg/mL, which is eight times higher than the concentration used for in vivo imaging [45]. This finding underscores the favorable cellular biocompatibility of HM-Lipo-ICG, confirming its suitability for safe use in both tumor imaging and therapeutic applications.

Next, the homologous targeting efficacy of HM-Lipo-ICG to G422 GBM cells was investigated using confocal laser scanning microscopy (CLSM) and flow cytometry. HM-Lipo-ICG, Lipo-ICG, BM-Lipo-ICG, and GM-Lipo-ICG were incubated with G422 cells for 2 h, followed by

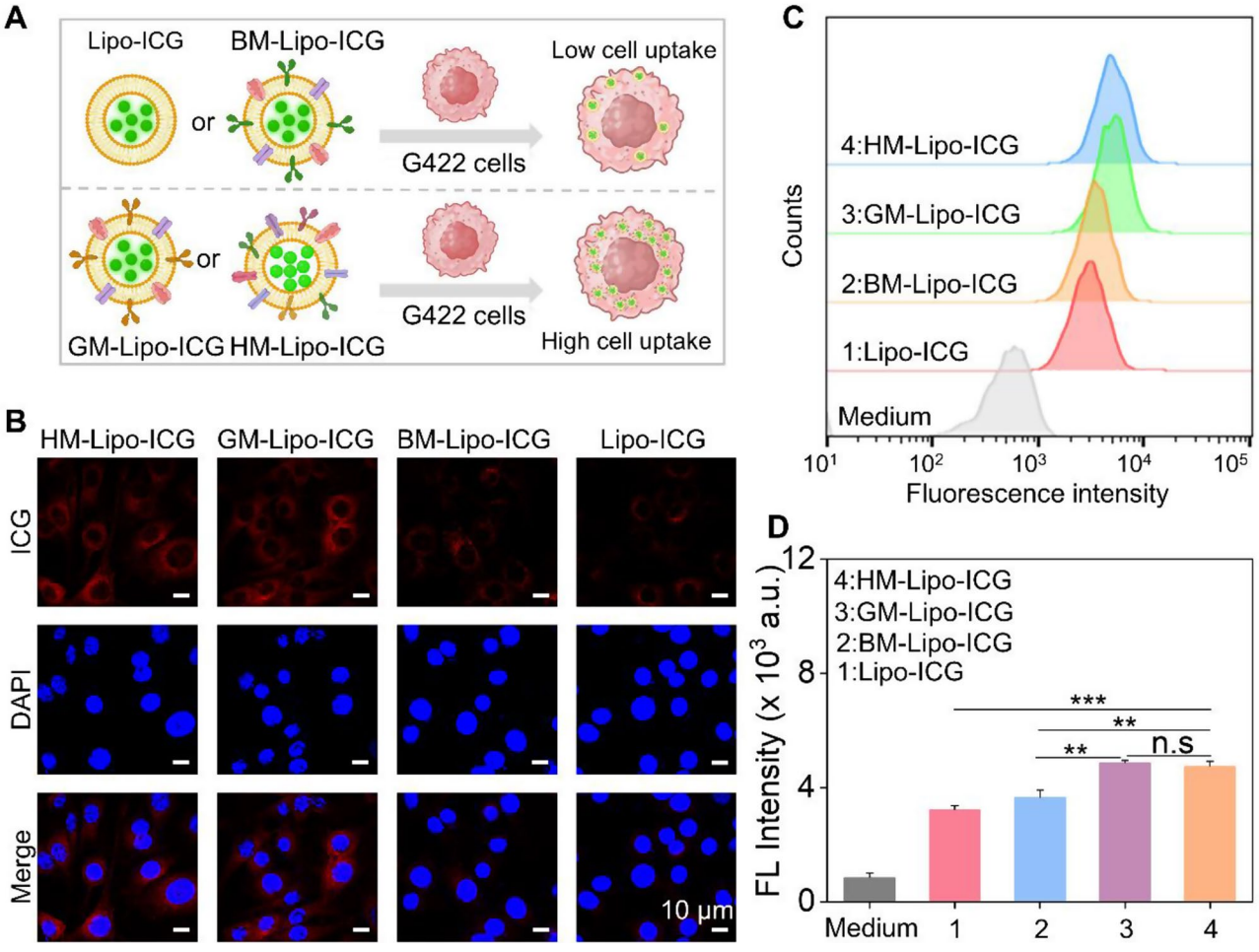

Fig. 3 Uptake of HM-Lipo-ICG by G422 glioma cells. **a**) Schematic of G422 glioma cell uptake of Lipo-ICG, BM-Lipo-ICG, GM-Lipo-ICG, and HM-Lipo-ICG. Image was created with BioRender.com, with permission.**b**) CLSM images of G422 glioma cells incubated with Lipo-ICG, BM-Lipo-ICG, GM-Lipo-ICG, and HM-Lipo-ICG for 2 h. Cell nuclei were stained with DAPI. C_{ICG} = 20 μg/mL. Scale bar = 10 μm. **c**) Flow cytometry analysis of G422 cell uptake of Lipo-ICG, BM-Lipo-ICG, GM-Lipo-ICG, and HM-Lipo-ICG. **d**) Mean fluorescence intensity of ICG in G422 glioma cells treated with Lipo-ICG, BM-Lipo-ICG, GM-Lipo-ICG, and HM-Lipo-ICG for 2 h ($n = 3$) in Fig. 3C. ns, ∗, ∗∗, and ∗∗∗ represent no statistical difference, $P < 0.05$, $P < 0.01$, and $P < 0.001$, respectively

fixation and DAPI staining (Fig. 3A). The results showed a distinct fluorescent signal from ICG (shown in red) in the HM-Lipo-ICG-treated and GM-Lipo-ICG-treated groups, indicating a significant increase in cellular uptake by G422 cells (Fig. 3B). This observation underscores the commendable self-recognition capacity of HM-Lipo-ICG and GM-Lipo-ICG towards homologous cells, a crucial aspect for achieving targeted cancer cell capabilities [46, 47]. Quantitative analysis by flow cytometry revealed that the average fluorescence intensity in HM-Lipo-ICG and GM-Lipo-ICG-treated cells exceeded that in Lipo-ICG-treated G422 cells by a factor of 1.5 (Fig. 3C and D). This further substantiates that HM-Lipo-ICG and GM-Lipo-ICG, by inheriting cell membrane proteins from G422 cells, efficiently enter glioma sites through homologous targeting.

Additionally, to comprehensively evaluate the performance of HM-Lipo-ICG in a realistic GBM brain condition, an in vitro BBB model was established by seeding endothelial cells in the upper chamber and GBM cells in the lower chamber (Fig. S7A). Subsequently, HM-Lipo-ICG, GM-Lipo-ICG, and Lipo-ICG were separately introduced into the upper chamber to assess their ability to penetrate the BBB and be taken up by glioma cells using confocal laser scanning microscopy (CLSM). The results obtained from CLSM imaging (Fig. S7B) and quantitative analysis (Fig. S7C) demonstrated that the group treated with HM-Lipo-ICG exhibited superior BBB penetration and active-targeting capabilities compared to both the GM-Lipo-ICG-treated group and Lipo-ICG-treated group. These findings highlight that through modification with homologous cell membrane, hybrid cell membrane camouflaged Lipo-ICG demonstrates excellent tumor targeting abilities after crossing the BBB (Fig. S7).

Finally, to assess whether the coating of tumor cell membranes protects against phagocytosis by macrophages, the cellular uptake of HM-Lipo-ICG by RAW264.7 cells was investigated using CLSM and flow cytometry. The results revealed that Lipo-ICG-treated cells exhibited increased red luminescence, whereas HM-Lipo-ICG-incubated cells showed a 1.5-fold reduction in intracellular fluorescence (Fig. S8). This suggests that only a minimal number of cell membrane-coated liposomes are internalized by RAW264.7 macrophages, underscoring the enhanced phagocytosis-evading capabilities conferred by the biofunctional properties inherited from the source cancer cells [46, 48].

In Vivo targeted BBB penetration of HM-Lipo-ICG

Encouraged by the successful traversal of the in vitro Transwell BBB by HM-Lipo-ICG, we further evaluated the ability of HM-Lipo-ICG to penetrate the BBB and enter brain tissue in a normal mouse model using NIR fluorescence imaging. Four different liposomal formulations, including HM-Lipo-ICG, Lipo-ICG, GM-Lipo-ICG, and BM-Lipo-ICG, were administered *via* intravenous injection (1.0 mg/kg per mouse), and real-time NIR fluorescence imaging was performed at various time points. As illustrated in Fig. 4A, the groups injected with Lipo-ICG and GM-Lipo-ICG exhibited minimal fluorescence signals in the brain regions of healthy mice. In stark contrast, the groups receiving BM-Lipo-ICG and HM-Lipo-ICG showed significantly higher fluorescent signals, confirming that the use of metastatic cancer cell membrane camouflage conferred exceptional BBB permeability to the liposomes, allowing them to penetrate the brain even when the BBB was intact. Quantitative analysis revealed that, at 6 h post-injection, the fluorescence intensity in the brains of mice treated with HM-Lipo-ICG and BM-Lipo-ICG was approximately 2.8 times higher compared to those treated with Lipo-ICG and GM-Lipo-ICG (Fig. 4B). No statistically significant difference in fluorescence intensity was observed between the Lipo-ICG and GM-Lipo-ICG groups, nor between the BM-Lipo-ICG and HM-Lipo-ICG groups. These findings suggest that cell membrane-coated biomimetic liposomes derived from brain metastatic cancer cells retain the functional properties of the original cell membrane, thus enhancing their BBB penetration capabilities. Additionally, ex vivo imaging of dissected brains corroborated the in vivo results, showing substantial fluorescent signals in the BM-Lipo-ICG and HM-Lipo-ICG groups (Fig. 4C).

In vivo imaging of infiltrative tumor margins

The G422 orthotopic glioma mouse model was established using methods previously described by our group [22]. This model was utilized to evaluate the in vivo and microscopic near-infrared (NIR) fluorescence imaging capabilities of HM-Lipo-ICG for visualizing tumor margins (Fig. 5A). Luciferase-stably transfected G422 cells exhibited strong bioluminescent signals in the mouse brain 9 days post-establishment (Fig. 5B and Fig S9). Gadolinium-based T1-weighted contrast-enhanced magnetic resonance imaging also delineated the brain tumor region in vivo (Fig. 5C). Furthermore, histopathological analysis of whole brain tissue from model mice using hematoxylin and eosin (H&E) staining revealed areas of infiltrative tumor margins within the brain tissue (Fig. 5D). These findings collectively confirm the successful establishment of an infiltrative GBM orthotopic mouse model.

Subsequently, the in vivo NIR fluorescence imaging capability of HM-Lipo-ICG for visualizing infiltrative tumor margins was assessed using the IVIS imaging system. Following intravenous injection of HM-Lipo-ICG (1.0 mg/kg per mouse), NIR fluorescence imaging was performed at various time points (Fig. 5E). The results demonstrated progressive fluorescence signals within the

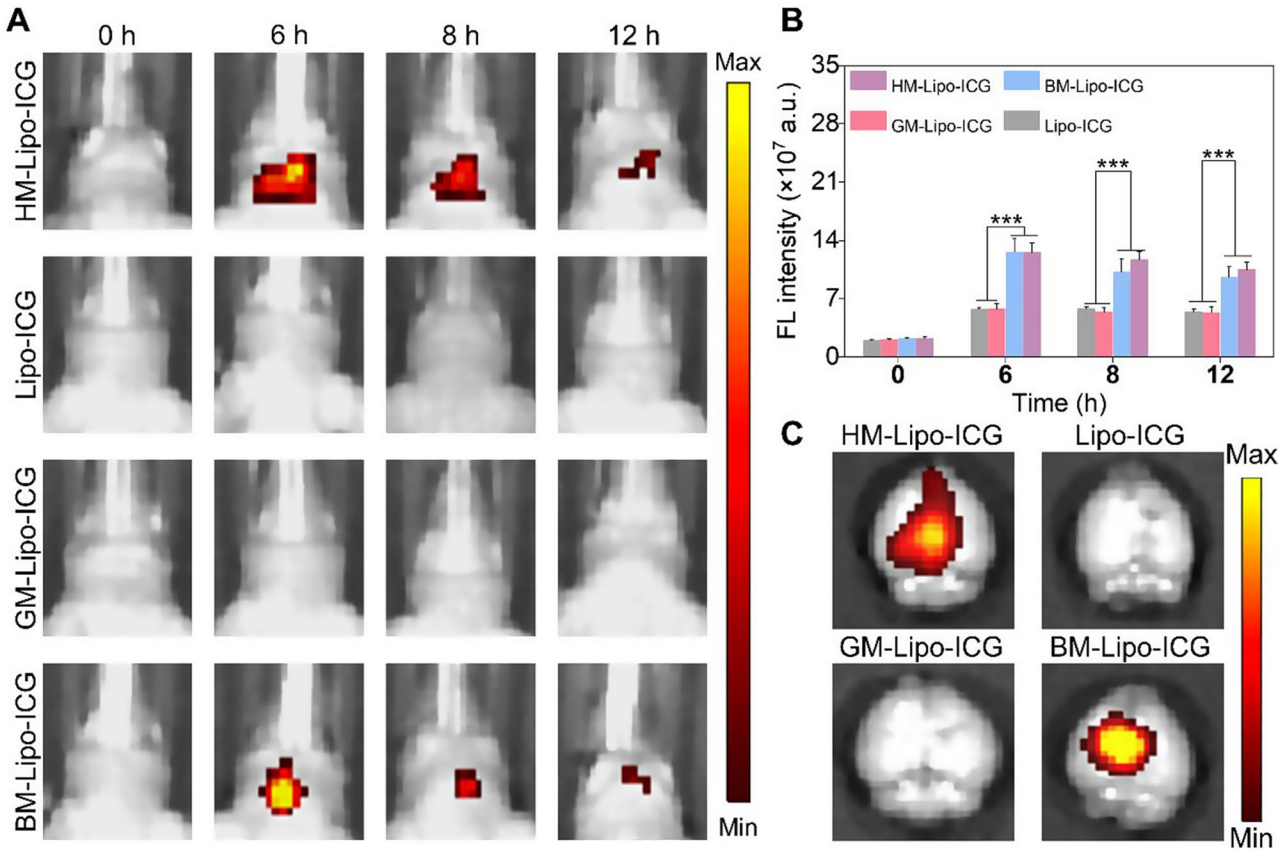

Fig. 4 HM-Lipo-ICG crossing the BBB in normal mice. **a**) NIR fluorescence imaging of normal mouse brains at various time points following intravenous injection of HM-Lipo-ICG at a dose of 1.0 mg/kg. **b**) Quantitative analysis of fluorescence intensity in mouse brains from Fig. 4A. $n = 3$. **c**) Ex vivo NIR fluorescence images of brain tissue from different treatment groups 6 h post-intravenous injection

brain tumor region in the HM-Lipo-ICG, BM-Lipo-ICG, and GM-Lipo-ICG treatment groups, peaking at 6 h post-injection before gradually declining. In contrast, minimal fluorescence was observed in the Lipo-ICG-treated group within the mouse brain. Quantitative analysis indicated that at 6 h post-injection, fluorescence intensity at the tumor sites of BM-Lipo-ICG and HM-Lipo-ICG-treated mice was approximately 1.4-fold and 1.9-fold higher, respectively, compared to Lipo-ICG-treated mice (Fig. 5F). Following Fig. 4A, the peak accumulation of HM-Lipo-ICG in the targeted tumor regions is indicated by the highest fluorescence intensity observed at 6 h post-injection. The decline in fluorescence intensity over time can be attributed to a combination of liposome clearance through lymphatic and circulatory systems, metabolic degradation, and potential cellular uptake. HM-Lipo-ICG enabled high-contrast NIR imaging with a signal-to-background ratio of 6.5 in GBM regions within the orthotopic glioma mouse model. Ex vivo imaging of brain tissues from different treatment groups corroborated the in vivo fluorescence imaging results (Fig. 5G), confirming the superior homotypic targeting ability of G422 glioma cell membrane-camouflaged liposomes. Importantly, fluorescence intensity in gliomas of the HM-Lipo-ICG-treated group was significantly greater than in the GM-Lipo-ICG and BM-Lipo-ICG-treated groups, underscoring that HM-Lipo-ICG nanoparticles effectively traverse the BBB surrounding emerging gliomas and exhibit specific tumor-targeting capabilities.

Additionally, NIR fluorescence microscopic imaging of HM-Lipo-ICG was employed to delineate infiltrative tumor margins in frozen sections of brain tissues. For this purpose, RFP-transfected G422 (RFP-G422) cells were used to establish orthotopic glioma mouse models. As depicted in Fig. 5H, brain tissue sections from the HM-Lipo-ICG-treated group showed complete overlap between red fluorescence emitted by glioma cells and green fluorescence emitted by ICG. In contrast, green fluorescence of ICG in the GM-Lipo-ICG-treated group did not fully correspond with red fluorescence at glioma margins, indicating that liposomes modified with hybrid cell membranes can more accurately identify infiltrative glioma margins compared to those modified with single glioma cell membranes. Further quantitative analysis (Fig. 5I, J) revealed that the agreement between tumor areas identified by the HM-Lipo-ICG-treated group and

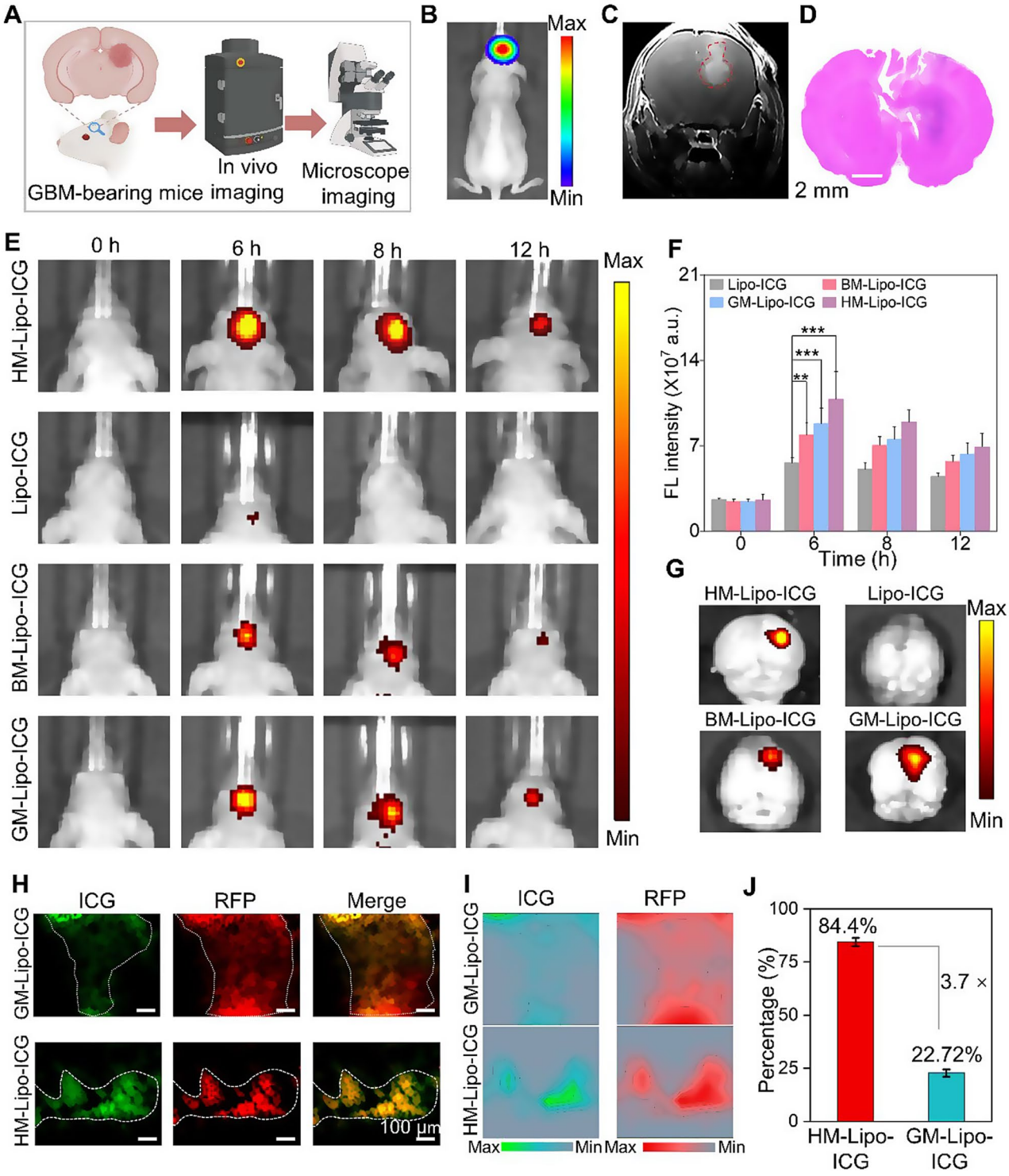

Fig. 5 HM-Lipo-ICG for accurate visualization of infiltrative tumor margins in an orthotopic glioma mouse model. **a**) Schematic of the G422 orthotopic glioma model construction and its application in fluorescence and microscopic NIR fluorescence imaging in vivo. **b**) A bioluminescence image and **c**) a magnetic resonance image of a G422 orthotopic glioma mouse. **d**) H&E-stained histological section of brain tissue of G422 glioma cells in mouse brains 9 days post-implantation. Scale bar = 10 μm. **e**) NIR fluorescence images of G422 tumor-bearing mice treated with Lipo-ICG, BM-Lipo-ICG, GM-Lipo-ICG, and HM-Lipo-ICG at various time points. Intravenous dose of ICG = 1.0 mg/kg. **f**) Quantitative analysis of fluorescence signal intensity in the mouse brain regions in Fig. 5E. **g**) Ex vivo fluorescence images of brain tissue 4 h post-injection of Lipo-ICG, BM-Lipo-ICG, GM-Lipo-ICG, and HM-Lipo-ICG. **h**) NIR fluorescence microscopy images of brain tumor Sect. 6 h post-injection of GM-Lipo-ICG and HM-Lipo-ICG, respectively. Scale bar = 10 μm. **i**) Quantitative fluorescence intensity distribution map of Fig. 5H. The map is obtained by extracting and normalizing the fluorescence intensity signals from Fig. 5D and projecting them onto the corresponding positions. Scale bar = 10 μm. **j**) Quantitative analysis of the results from Fig. 5I ($n = 3$)

actual tumor areas was as high as 84.4%, approximately 3.7 times higher than that of the GM-Lipo-ICG-treated group (22.7%).

Finally, the biodistribution and metabolic pathways of HM-Lipo-ICG in normal mice were evaluated. Ex vivo NIR fluorescence imaging (Fig S10) revealed that 6 h post-intravenous injection, HM-Lipo-ICG primarily accumulated in liver tissue, consistent with findings for Lipo-ICG, BM-Lipo-ICG, and GM-Lipo-ICG. However, signal intensity in liver tissue was lower in the HM-Lipo-ICG-treated group compared to the Lipo-ICG-treated group, suggesting that cell membrane modification can reduce reticuloendothelial system (RES) uptake of Lipo-ICG, thereby enhancing imaging quality.

Fluorescence image-guided surgical resection of GMB in vivo

HM-Lipo-ICG demonstrated a remarkable ability to identify infiltrative tumor margins, highlighting its potential for guiding fluorescence imaging-directed surgical resection. To assess its applicability in facilitating precise neurosurgery for GBM, craniotomies were performed with stepwise glioma tissue removal guided by NIR fluorescence imaging of HM-Lipo-ICG, as depicted in Fig. 6A. A representative brain bearing GBM was collected 6 h post-injection of HM-Lipo-ICG. The tumor region, highlighted by a blue circle in Fig. 6C, was exposed and subjected to sequential resections to excise GBM tissue. Before initial resection, the tumor protruded from the brain surface, emitting strong fluorescence signals (Fig. 6B). Following the first resection, the tumor mass visibly disappeared under direct observation, yet

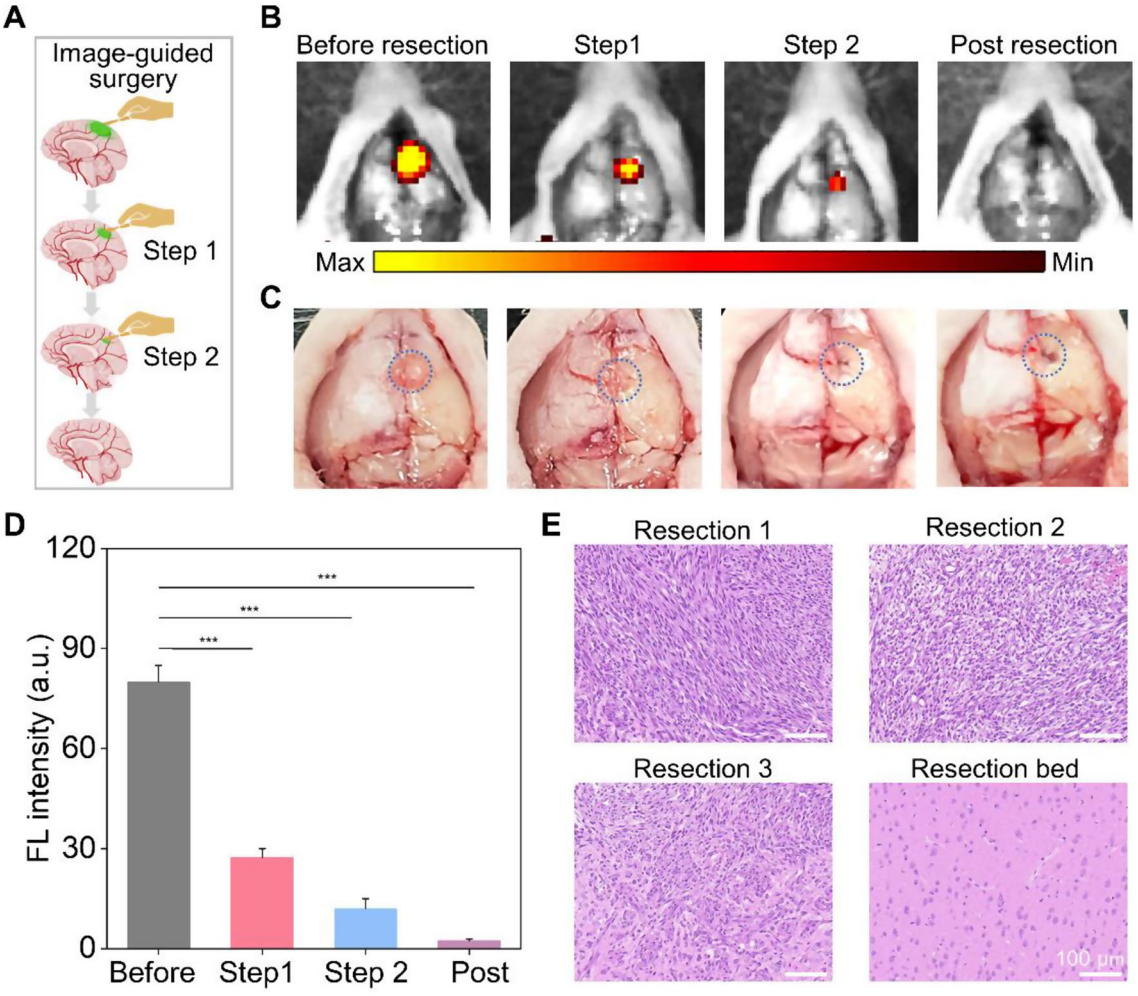

Fig. 6 In vivo NIR fluorescence imaging-guided glioma surgery in G422 orthotopic glioma models. **a**) Schematic representation of the stepwise surgical procedure. **b**) and **c**) Digital and NIR fluorescence images of the tumor resection site, taken 6 h post-injection of HM-Lipo-ICG nanoparticles. The blue dashed circle in Fig. 6C delineates the tumor location. The surgery continued until all regions emitting a bright fluorescent signal were completely excised. **d**) Quantitative analysis of fluorescence signal intensity in the mouse brain regions in Fig. 6B. **e**) Representative H&E-stained sections of the resected tumor tissues following each surgical stage. Scale bar = 100 μm

significant fluorescence persisted in the resection bed. Subsequently, a second resection removed remaining fluorescent tissue, creating a small cavity on the brain surface. However, a faint area of residual fluorescence was detected after the second resection, indicating a residual tumor in the surgical cavity. Therefore, a third resection was conducted, resulting in complete disappearance of fluorescence. Quantitative analysis revealed that stepwise glioma removal reduced fluorescence at the tumor site from 80.0 (pre-resection) to 27.4 (first resection), 12.0 (second resection), and ultimately to zero (Fig. 6D). To validate surgical outcomes, resected tissue was examined using hematoxylin and eosin (H&E) staining (Fig. 6E). Initial H&E staining of dissected tumor tissue revealed a dense population of tumor cells, gradually diminishing with successive resections. Following disappearance of fluorescence, the resection bed displayed normal brain tissue. These findings emphasize that HM-Lipo-ICG-based NIR fluorescence imaging represents a promising strategy for guiding precise and comprehensive neurosurgery, effectively targeting gliomas and delineating tumor margins.

In vivo toxicity evaluation

The in vivo cytotoxicity of Lipo-ICG, GM-Lipo-ICG, BM-Lipo-ICG, and HM-Lipo-ICG was rigorously assessed through a comprehensive analysis of blood biochemistry. Mice treated with PBS as the control. Results showed that the mice treated with nanoparticles exhibited negligible changes in three key liver function markers compared to the control group (Fig. S11), including alanine aminotransferase (ALT), aspartate aminotransferase (AST), and alkaline phosphatase (ALP). Additionally, routine blood parameters, including red blood cell (RBC) count, white blood cell (WBC) count, hematocrit (HCT), mean corpuscular volume (MCV), hemoglobin (HGB), and platelet count (PLT), showed no significant differences between groups. These findings underscore the favorable in vivo biosafety of these nanoparticles, without inducing distinct liver or renal toxicity. Histopathological examination from H&E-stained slices of major organs (heart, liver, lung, spleen, and kidney) also revealed no discernible pathological tissue changes or damage in the different treated groups compared with the control group (Fig. S12), indicating the absence of side effects or toxicities induced by these liposomes or cell membrane coating. Taken together, these results confirm that HM-Lipo-ICG exhibits excellent biosafety and that the hybrid tumor cell membrane cloaked strategy did not affect the normal function of the human tissues, holding significant promise for clinical application.

Conclusions

In conclusion, our study demonstrates the successful development of hybrid cell membrane-coated ICG liposomes (HM-Lipo-ICG) for targeted BBB penetration and precise imaging of infiltrative GBM margins. HM-Lipo-ICG achieved superior BBB traversal and tumor targeting through CD44 receptor-mediated endocytosis and homotypic targeting, significantly enhancing the accuracy of fluorescence-guided surgical resection. The HM-Lipo-ICG exhibited remarkable stability, biocompatibility, and safety, making them a promising tool for improving GBM surgical outcomes. This biomimetic approach offers a novel strategy for the precise visualization and complete resection of infiltrative tumors, potentially reducing postoperative recurrence and prolonging patient survival.

Materials and methods

Materials

The lipids 1,2-Dioleoyl-sn-glycero-3-phosphocholine (DOPC) and 1,2-distearoyl-sn-glycero-3-phosphoethanolamine-N-[amino(polyethylene glycol)] (DSPE-PEG) were obtained from Avanti Polar Lipids in Alabaster, Birmingham, AL, USA. Indocyanine green (ICG) was acquired from Sigma-Aldrich located in St. Louis, MO, USA. Cell culture reagents such as penicillin-streptomycin, trypsin-EDTA, fetal bovine serum (FBS), phosphate-buffered saline (PBS), high-glucose DMEM and RPMI 1640 medium were sourced from Gibco at Thermo Fisher Scientific based in Waltham, MA, USA. The membrane protein extraction kit, bicinchoninic acid protein assay kit (BCA) along with phenylmethylsulfonyl fluoride (PMSF), and the Cell Counting Kit-8 (CCK-8) assay were supplied by Beyotime Biotechnology situated in Shanghai China. All other reagents utilized were of analytical grade. Reagents for western blotting (WB) tests and histological studies were purchased from Yaenzyme (China).

Cell culture

Mouse-derived melanoma cells (B16F10) were cultured in RPMI 1640 medium, while mouse-derived glioblastoma cells expressing luciferase (G422-Luc) and mouse-derived macrophage cells (RAW 264.7) were maintained in high-glucose DMEM medium. All culture media contained 10% fetal bovine serum (FBS) and 1% antibiotics (100 units/mL penicillin and 100 micrograms/mL streptomycin). The cells were incubated at a temperature of 37 °C with a CO_2 concentration of 5% in a humidified environment.

Preparation of HM-Lipo-ICG NPs

Synthesis of Lipo-ICG

A thin-film hydration technique was employed to synthesize Lipo-ICG. Initially, a solution containing 5 mg

DOPC and 1 mg DSPE-PEG_{2000} (in a molar ratio of 95:5) was dissolved in chloroform ($CHCl_3$). Subsequently, the solution underwent rotary evaporation followed by vacuum drying for 4 h, resulting in the formation of a thin lipid film. The dried film was then rehydrated using an aqueous ICG solution with a concentration of 300 μg/mL at a weight ratio of 1:40 (ICG to phospholipid). After rehydration, the mixture experienced five cycles of freezing and thawing, alternating between liquid nitrogen and a water bath at 65 °C. Finally, the resultant liposomal suspension was extruded through polycarbonate membranes with pore sizes measuring both 200 nm and 100 nm respectively for a total number of twenty passes each to obtain Lipo-ICG.

Preparation of the hybrid cell membranes

The B16F10 and G422 cells were collected and suspended in a hypotonic lysing buffer containing membrane protein extraction reagent and phenylmethylsulfonyl fluoride (PMSF). The suspension was then placed in an ice bath for 15 min and subjected to three cycles of freeze-thaw technique, involving multiple cycles of freezing and thawing between a room-temperature water bath (37℃) and liquid nitrogen. Following this, the cells were centrifuged at 700 g for 10 min at 4 °C. The resulting supernatant was collected and further centrifuged at 14,000 g for 30 min at -80 °C. The resulting white precipitate was resuspended in deionized water and stored at -80 °C for subsequent experiments.

The concentration of B16F10 and G422 membrane proteins was determined using a protein assay kit. B16F10 cell membranes were combined with G422 cell membranes in equal weight proportions of membrane proteins (1:1). These mixed membranes were extruded through a polycarbonate membrane with pores measuring approximately 400 nm to create hybrid cell membranes.

To confirm the successful fusion of B16F10 and G422 cell membranes, FITC-labeled B16F10 membranes and Cy5-labeled G422 membranes respectively underwent extrusion to fabricate HM-Lipo-ICG which was then introduced to perfluoropropane followed by vigorous shaking. The labeled B16F10/G422 cell membranes as well as the hybrid membranes were subsequently observed using confocal laser scanning microscopy (CLSM).

The fabrication process of biomimetic HM-Lipo-ICG involved the application of hybrid membranes (HM) for coating Lipo-ICG at a weight ratio of 1:300 (protein to phospholipid). This was achieved by manually extruding the mixture through polycarbonate membranes with pore sizes of 200 nm and 100 nm, repeated a total of 11 times.

Characterization of HM-Lipo-ICG NPs

The hydrodynamic size and zeta potential of the samples were determined using dynamic light scattering (Zetasizer Nano ZS, Malvern, United Kingdom), while transmission electron microscopy (TEM) was utilized to examine the morphology of the NPs. The encapsulation efficiency (EE) and loading capacity (LC) of ICG were evaluated by using a UV spectrophotometer (PerkinElmer LAMBDA 25, USA). The EE and LC were calculated as described below ($n=3$).

$$\text{Encapsulation Efficiency of ICG } (\%) = \frac{\text{ICG encapsulated in HM-Lipo-ICG}}{\text{Total ICG added}} \times 100\%$$

$$\text{Loading capacity of ICG}\,(\%) = \frac{\text{ICG encapsulated in HM-Lipo- ICG}}{\text{Weight of HM-LipoICG}} \times 100\%$$

To assess the retention of membrane proteins on BM-Lipo-ICG, GM-Lipo-ICG, and HM-Lipo-ICG, SDS-PAGE analysis was performed. Additionally, the western blotting analysis was conducted to assess the expression of the CD44 on BM-Lipo-ICG and HM-Lipo-ICG. The concentration of ICG in the samples was also quantified by measuring absorbance at 792 nm using a UV spectrophotometer (PerkinElmer LAMBDA 25, USA). UV-visible-NIR spectra were recorded, and fluorescence emission spectra were obtained with an excitation wavelength of 720 nm using a fluorescence spectrophotometer (F900, Edinburgh Instruments Ltd., UK). Furthermore, DLS measurements were employed to monitor changes in diameter as an indicator for assessing stability in water, PBS, and 10% FBS solutions.

Cellular uptake by flow cytometry and confocal microscopy

The uptake of the nanoprobes was evaluated using CLSM and flow cytometry. G422, bEnd.3, and RAW 264.7 cells were seeded in 24-well plates with a density of 1×10^5 cells per well and incubated for 24 h. Following that, the cells were exposed to Lipo-ICG, GM-Lipo-ICG, and HM-Lipo-ICG at a concentration of 20 μg/mL for 4 h at a temperature of 37 °C. Subsequently, the cells were washed with PBS, collected and analyzed using flow cytometry (APC-A700 channel).

For intracellular distribution and localization of the nanoprobes, G422, bEnd.3, and RAW 264.7 cells (1×10^5 cells per dish) were plated on glass-bottom dishes (35 mm) dish and cultured at 37 °C for 24 h. Then, the cells were incubated with the nanoparticles (at an ICG concentration of 20 μg/mL) for 4 h. After washing with PBS, and fixing with 4% paraformaldehyde, the cell nuclei were stained with DAPI for 15 min and imaged using CLSM (LeicaTCS-SP8STED; Heidelberg Germany).

In vitro cytotoxicity evaluation

The CCK-8 assay was used to evaluate the cytotoxicity of Lipo-ICG, GM-Lipo-ICG, BM-Lipo-ICG, and HM-Lipo-ICG. In brief, cells were cultured in 96-well plates (1×10^4 cells per well) at 37 °C for 24 h. Then, different formulations and concentrations of samples including Lipo-ICG and BM/GM/HM-Lipo-ICG (with an ICG concentration of 20 μg/mL) were added to the cells and incubated for another 24 h at 37 °C. After washing with PBS, CCK-8 reagent (10 μL per every 100 μL of DMEM) was added to each well. The cultures were further incubated for an additional 4 hours before measuring the absorbance value at a wavelength of 450 nm to determine cell viability in G422 and bEnd.3 cells.

In vitro BBB model

An in vitro model of the blood-brain barrier (BBB) was established using bEnd.3 cells in a transwell cell culture system. Tight junctions were formed by refreshing the medium every other day. The integrity of the BBB model was evaluated by measuring transepithelial electrical resistance (TEER) with a CellZscope system (NanoAnalytics, Germany).

Various nanoparticles containing 20 μg/mL of ICG were introduced into the upper chamber and incubated for 4 h. Subsequently, the supernatant from the upper and lower chamber was collected. The distribution and penetration of nanoparticles across BBB were determined by quantifying fluorescence intensity of ICG in each compartment relative to its initial concentration.

Animals and orthotopic glioma model

Female BALB/c nude mice weighing 18–22 g and aged 6–8 weeks were obtained from Beijing Vital River Laboratory Animal Technology Co., Ltd. (China) and housed in a sterile environment at room temperature, following a 12-hour light/dark cycle. They were provided with unrestricted access to food and water. All animal procedures adhered to the protocols approved by the Animal Care and Use Committee at the Shenzhen Institutes of Advanced Technology, Chinese Academy of Sciences.

To establish an intracranial orthotopic glioma model, G422 cells were injected into the striatum region of the mice's brains. The animals were anesthetized using avertin gas-oxygen-ether anesthesia and secured in a stereotactic frame for precise positioning. Approximately 5.0×10^5 G422 cells (Luciferase-stably transfected G422 cells or RFP-transfected G422 cells), suspended in 5 μL of serum-free medium, were implanted into the right striatum at specific coordinates: right lateral position at 1.0 mm from bregma point, with a depth of insertion set at 3.25 mm below the brain surface. Glioma growth was monitored through bioluminescence and fluorescence imaging.

In vivo fluorescence imaging in orthotopic glioma

After establishing the orthotopic glioma mouse model successfully, Lipo-ICG and BM/GM/HM-Lipo-ICG (ICG concentration: 0.5 mg/kg) were intravenously administered to the glioma-bearing mice. In vivo fluorescent images were captured at baseline, 6 h, 8 h, and 12 h post-injection using the IVIS Spectrum imaging system (PerkinElmer, United States). Mice were euthanized at 6 h post-injection, and organs (liver, kidney, spleen, heart, lung) along with brains were harvested for ex vivo fluorescence imaging.

Fluorescence-guided glioma surgery in vivo

At 6 h post-injection of the HM-Lipo-ICG probe, mice were euthanized, and fluorescence-guided glioma surgery was conducted on an operating platform. The mouse skin was dissected to fully expose the cranial bone, which was then carefully separated using forceps to expose the brain tissue. Before resection, fluorescence imaging was performed. Initial resection was guided visually, followed by another round of fluorescence imaging to assess the surgical bed. Subsequently, a second surgery was conducted based on real-time feedback from the in vivo fluorescence signal at the cutting edge. A third resection was performed if the fluorescence signal persisted, continuing until the signal disappearance. Resected tumor samples and selected surgical bed samples without fluorescence signal were collected and confirmed *via* H&E staining.

In vivo safety evaluation

The biosafety of nanoparticles was assessed through a comprehensive evaluation involving histological staining, blood routine analysis, and serological tests. BALB/c mice ($n=3$) were intravenously administered BM/GM/HM-Lipo-ICG at a concentration of 1 mg/kg. Mice treated with PBS served as the control group. Twenty-four hours post-injection, the animals were euthanized, and blood samples along with major organs (heart, liver, spleen, lung, kidney, and brain) were collected for subsequent blood tests and histological examination.

Liver and kidney function were evaluated by measuring key biomarkers: alanine aminotransferase (ALT), aspartate aminotransferase (AST), and alkaline phosphatase (ALP) using a blood biochemistry analyzer. Additionally, a complete blood count was performed to determine red blood cell count (RBC), white blood cell count (WBC), hematocrit (HCT), mean corpuscular volume (MCV), hemoglobin (HGB), and platelet count (PLT) using an autoanalyzer.

For histological analysis, major organs were fixed in 4% paraformaldehyde, embedded in paraffin, and sectioned. The sections were stained with hematoxylin and eosin (H&E) and subsequently examined and imaged using an optical microscope.

Statistical analysis

Statistical analysis was performed using SPSS 26 software (IBM, Endicott, NY). Data were expressed as mean ± standard deviation (SD). Significance between two groups was evaluated using Student's t-test. One-way analysis of variance (ANOVA) was employed for comparisons among multiple groups. A p-value less than 0.05 was considered statistically significant ($^{*}p<0.05$, $^{**}p<0.01$, $^{***}p<0.005$), while "NS" denoted no statistically significant difference.

Supplementary Information

The online version contains supplementary material available at https://doi.org/10.1186/s12951-024-02870-1.

Supplementary Material 1

Acknowledgements

This study is supported by the National Key Research and Development Program of China (No. 2023YFF0714200), the Natural Science Foundation of China (82102004, 82271948, 92159304, 82372022, 82227806, 82171958), Science and Technology Planning Project of Guangzhou (2023A03J0276), Shenzhen Medical Research Funds (B2302021, E3A1051001), Guangdong Basic and Applied Basic Research Fund (Grant Nos.2024A1515030212, 2023A1515010747, 2023A1515140133, 2022A1515140102).We also thank the BioRender.com for permission of figures.

Author contributions

Zonghai Sheng and Guihua Jiang have made substantial contributions to the conception and design of the work. Ping Liu and Siyi Lan contributed equally to the acquisition and analysis. Dehong Hu and Duyang Gao contributed to the interpretation of data. Zhen Chen and Ziyue Liu contributed to analysis.

Data availability

Data is provided within the manuscript or supplementary information files.

Declarations

Ethics approval and consent to participate

All animal experiments were approved and performed by the Animal Care and Use Committee of Shenzhen Institutes of Advanced Technology, Chinese Academy of Sciences (China) and also in accordance with the policy of the National Institute of Health (China).

Consent for publication

All authors agree for publication. Part of the schematic images were created with BioRender.com, with permission.

Competing interests

The authors declare no competing interests.

Author details

[1]Department of Medical Imaging, The Affiliated Guangdong Second Provincial General Hospital of Jinan University, #466 Xingang Middle Road, Haizhu District, Guangzhou 510317, P. R. China
[2]Research Center for Advanced Detection Materials and Medical Imaging Devices, Institute of Biomedical and Health Engineering, Shenzhen Institute of Advanced Technology, Chinese Academy of Sciences, Shenzhen 518055, P. R. China
[3]The Key Laboratory of Biomedical Imaging Science and System, Chinese Academy of Sciences, Shenzhen 518055, P. R. China

Received: 27 July 2024 / Accepted: 23 September 2024
Published online: 05 October 2024

References

1. Louis DN, Perry A, Wesseling P, Brat DJ, Cree IA, Figarella-Branger D, et al. The 2021 WHO classification of tumors of the central nervous system: a summary. Neuro Oncol. 2021;23(8):1231–51.
2. Molinaro AM, Hervey-Jumper S, Morshed RA, Young J, Han SJ, Chunduru P, et al. Association of maximal extent of resection of contrast-enhanced and non-contrast-enhanced tumor with survival within molecular subgroups of patients with newly diagnosed glioblastoma. JAMA Oncol. 2020;6(4):495–503.
3. Shen B, Zhang Z, Shi X, Cao C, Zhang Z, Hu Z, et al. Real-time intraoperative glioma diagnosis using fluorescence imaging and deep convolutional neural networks. Eur J Nucl Med Mol Imaging. 2021;48(11):3482–92.
4. Kircher MF, de la Zerda A, Jokerst JV, Zavaleta CL, Kempen PJ, Mittra E, et al. A brain tumor molecular imaging strategy using a new triple-modality MRI-photoacoustic-raman nanoparticle. Nat Med. 2012;18(5):829–34.
5. Zhao H, Li C, Shi X, Zhang J, Jia X, Hu Z, et al. Near-infrared II fluorescence-guided glioblastoma surgery targeting monocarboxylate transporter 4 combined with photothermal therapy. EBioMedicine. 2024;106:105243.
6. Refaat A, Yap ML, Pietersz G, Walsh APG, Zeller J, Del Rosal B, et al. In vivo fluorescence imaging: success in preclinical imaging paves the way for clinical applications. J Nanobiotechnol. 2022;20(1):450.
7. Cheng Z, Jin Y, Li J, Shi G, Yu L, Shao B, et al. Fibronectin-targeting and metalloproteinase-activatable smart imaging probe for fluorescence imaging and image-guided surgery of breast cancer. J Nanobiotechnol. 2023;21(1):112.
8. Surface-enhanced Raman spectroscopy. Nat Reviews Methods Primers. 2022;1(1):86.
9. Jin Z, Yue Q, Duan W, Sui A, Zhao B, Deng Y, et al. Intelligent SERS Navigation System guiding brain tumor surgery by Intraoperatively delineating the metabolic acidosis. Adv Sci (Weinh). 2022;9(7):e2104935.
10. Gao X, Yue Q, Liu Z, Ke M, Zhou X, Li S et al. Guiding brain-tumor surgery via blood-brain-barrier-permeable gold nanoprobes with acid-triggered MRI/SERRS signals. Adv Mater. 2017;29(21).
11. Zheng S, Zhang Z, Qu Y, Zhang X, Guo H, Shi X, et al. Radiopharmaceuticals and Fluorescein Sodium Mediated Triple-Modality Molecular Imaging allows precise image-guided tumor surgery. Adv Sci (Weinh). 2019;6(13):1900159.
12. Bortot B, Mangogna A, Di Lorenzo G, Stabile G, Ricci G, Biffi S. Image-guided cancer surgery: a narrative review on imaging modalities and emerging nanotechnology strategies. J Nanobiotechnol. 2023;21(1):155.
13. He P, Xiong Y, Ye J, Chen B, Cheng H, Liu H, et al. A clinical trial of super-stable homogeneous lipiodol-nanoICG formulation-guided precise fluorescent laparoscopic hepatocellular carcinoma resection. J Nanobiotechnol. 2022;20(1):250.
14. Sheng Z, Hu D, Xue M, He M, Gong P, Cai L. Indocyanine Green nanoparticles for Theranostic Applications. Nano-Micro Lett. 2013;5(3):145–50.
15. Le QV, Kang S, Lee J, Park H, Sun JG, Lee J, et al. Size-dependent effect of Indocyanine Green Nanoimaging Agent for metastatic lymph node detection. Biomater Res. 2024;28:0022.
16. Shaw TK, Paul P. Recent approaches and success of liposome-based nano drug carriers for the treatment of brain tumor. Curr Drug Deliv. 2022;19(8):815–29.
17. Kim M, Hwang JE, Lee JS, Park J, Oh C, Lee S, et al. Development of Indocyanine Green/Methyl-β-cyclodextrin complex-loaded liposomes for enhanced Photothermal Cancer Therapy. ACS Appl Mater Interfaces. 2024;16(26):32945–56.
18. Xiong X, Li J, Gao D, Sheng Z, Zheng H, Liu W. Cell-membrane biomimetic indocyanine green liposomes for phototheranostics of echinococcosis. Biosens (Basel). 2022;12(5).
19. Gao D, Luo Z, He Y, Yang L, Hu D, Liang Y, et al. Low-dose NIR-II preclinical bioimaging using liposome-encapsulated cyanine dyes. Small. 2023;19(17):e2206544.
20. Cheung CCL, Ma G, Karatasos K, Seitsonen J, Ruokolainen J, Koffi CR, et al. Liposome-Templated Indocyanine Green J- aggregates for in vivo Near-Infrared imaging and stable Photothermal Heating. Nanotheranostics. 2020;4(2):91–106.
21. Xu HL, Shen BX, Lin MT, Tong MQ, Zheng YW, Jiang X, et al. Homing of ICG-loaded liposome inlaid with tumor cellular membrane to the homologous xenografts glioma eradicates the primary focus and prevents lung metastases through phototherapy. Biomater Sci. 2018;6(9):2410–25.
22. Jia Y, Wang X, Hu D, Wang P, Liu Q, Zhang X, et al. Phototheranostics: active targeting of Orthotopic Glioma using Biomimetic Proteolipid nanoparticles. ACS Nano. 2019;13(1):386–98.

23. Liu WS, Wu LL, Chen CM, Zheng H, Gao J, Lu ZM, et al. Lipid-hybrid cell-derived biomimetic functional materials: a state-of-the-art multifunctional weapon against tumors. Mater Today Bio. 2023;22:100751.
24. Hu CM, Zhang L, Aryal S, Cheung C, Fang RH, Zhang L. Erythrocyte membrane-camouflaged polymeric nanoparticles as a biomimetic delivery platform. Proc Natl Acad Sci U S A. 2011;108(27):10980–5.
25. Chen HY, Deng J, Wang Y, Wu CQ, Li X, Dai HW. Hybrid cell membrane-coated nanoparticles: a multifunctional biomimetic platform for cancer diagnosis and therapy. Acta Biomater. 2020;112:1–13.
26. Zhu L, Zhong Y, Wu S, Yan M, Cao Y, Mou N, et al. Cell membrane camouflaged biomimetic nanoparticles: focusing on tumor theranostics. Mater Today Bio. 2022;14:100228.
27. Wu H, Zhang T, Li N, Gao J. Cell membrane-based biomimetic vehicles for effective central nervous system target delivery: insights and challenges. J Control Release. 2023;360(7):169–84.
28. Chi S, Wang C, Liu Z. Biomimetic nanocomposites for Glioma Imaging and Therapy. Chemistry. 2024;30(31):e202304338.
29. Ma Y, Yi J, Ruan J, Ma J, Yang Q, Zhang K, et al. Engineered Cell membrane-coated nanoparticles: New Strategies in Glioma targeted therapy and Immune Modulation. Adv Healthc Mater. 2024;13(20):e2400514.
30. Mitusova K, Peltek OO, Karpov TE, Muslimov AR, Zyuzin MV, Timin AS. Overcoming the blood-brain barrier for the therapy of malignant brain tumor: current status and prospects of drug delivery approaches. J Nanobiotechnol. 2022;20(1):412.
31. Chen Z, Zhao P, Luo Z, Zheng M, Tian H, Gong P, et al. Cancer Cell membrane-biomimetic nanoparticles for homologous-targeting dual-modal imaging and Photothermal Therapy. ACS Nano. 2016;10(11):10049–57.
32. Li S, Meng X, Peng B, Huang J, Liu J, Xiao H, et al. Cell membrane-based biomimetic technology for cancer phototherapy: mechanisms, recent advances and perspectives. Acta Biomater. 2024;174:26–48.
33. Jiang Y, Krishnan N, Zhou J, Chekuri S, Wei X, Kroll AV, et al. Engineered cell-membrane-coated nanoparticles directly Present Tumor antigens to promote anticancer immunity. Adv Mater. 2020;32(30):e2001808.
34. Chi S, Zhang L, Cheng H, Chang Y, Zhao Y, Wang X, et al. Biomimetic nanocomposites camouflaged with hybrid cell membranes for Accurate Therapy of Early-Stage Glioma. Angew Chem Int Ed Engl. 2023;62(29):e202304419.
35. Kleffman K, Levinson G, Rose IVL, Blumenberg LM, Shadaloey SAA, Dhabaria A, et al. Melanoma-secreted amyloid Beta suppresses neuroinflammation and promotes Brain Metastasis. Cancer Discov. 2022;12(5):1314–35.
36. Wang Y, Pang J, Wang Q, Yan L, Wang L, Xing Z, et al. Delivering antisense oligonucleotides across the blood-brain barrier by Tumor Cell-Derived Small apoptotic bodies. Adv Sci (Weinh). 2021;8(13):2004929.
37. Wang C, Wu B, Wu Y, Song X, Zhang S, Liu Z. Camouflaging nanoparticles with brain metastatic tumor cell membranes: a New Strategy to Traverse blood–brain barrier for imaging and therapy of brain tumors. Adv Funct Mater. 2020;30(14):1909369.
38. Miao T, Ju X, Zhu Q, Wang Y, Guo Q, Sun T, et al. Nanoparticles surmounting blood–brain Tumor Barrier through both transcellular and paracellular pathways to Target Brain metastases. Adv Funct Mater. 2019;29(27):1900259.
39. Hao W, Cui Y, Fan Y, Chen M, Yang G, Wang Y, et al. Hybrid membrane-coated nanosuspensions for multi-modal anti-glioma therapy via drug and antigen delivery. J Nanobiotechnol. 2021;19(1):378.
40. Molinaro R, Corbo C, Martinez JO, Taraballi F, Evangelopoulos M, Minardi S, et al. Biomimetic proteolipid vesicles for targeting inflamed tissues. Nat Mater. 2016;15(9):1037–46.
41. Liu J, Gao D, Hu D, Lan S, Liu Y, Zheng H, et al. Delivery of Biomimetic liposomes via Meningeal Lymphatic Vessels Route for targeted therapy of Parkinson's Disease. Res (Wash D C). 2023;6:0030.
42. Zer NS, Ben-Ghedalia-Peled N, Gheber LA, Vago R. CD44 in bone metastasis development: a key player in the fate decisions of the invading cells? Clin Exp Metastasis. 2023;40(2):125–35.
43. Manten-Horst E, Danen EH, Smit L, Snoek M, Le Poole IC, Van Muijen GN, et al. Expression of CD44 splice variants in human cutaneous melanoma and melanoma cell lines is related to tumor progression and metastatic potential. Int J Cancer. 1995;64(3):182–8.
44. Xia Y, Zou C, Kang W, Xu T, Shao R, Zeng P, et al. Invasive metastatic tumor-camouflaged ROS responsive nanosystem for targeting therapeutic brain injury after cardiac arrest. Biomaterials. 2024;311:122678.
45. Hansen DA, Spence AM, Carski T, Berger MS. Indocyanine green (ICG) staining and demarcation of tumor margins in a rat glioma model. Surg Neurol. 1993;40(6):451–6.
46. Zhu JY, Zheng DW, Zhang MK, Yu WY, Qiu WX, Hu JJ, et al. Preferential Cancer Cell Self-Recognition and Tumor Self-Targeting by Coating nanoparticles with Homotypic Cancer cell membranes. Nano Lett. 2016;16(9):5895–901.
47. Sun H, Su J, Meng Q, Yin Q, Chen L, Gu W, et al. Cancer-Cell-Biomimetic nanoparticles for targeted therapy of homotypic tumors. Adv Mater. 2016;28(43):9581–8.
48. Li L, Zhang M, Li J, Liu T, Bao Q, Li X, et al. Cholesterol removal improves performance of a model biomimetic system to co-deliver a photothermal agent and a STING agonist for cancer immunotherapy. Nat Commun. 2023;14(1):5111.

Publisher's note